PAPER

Check for updates

A robust starch–polyacrylamide hydrogel with scavenging energy harvesting capacity for efficient solar thermoelectricity–freshwater cogeneration†

Xiaojiang Mu,[a] Jianhua Zhou,[a] Pengfei Wang,[b] Huan Chen,[a] Tingting Yang,[a] Siyi Chen,[c] Lei Miao [ID] *[a] and Takao Mori [ID] *[de]

The simultaneous production of clean water and electricity using solar energy has been proposed as a promising solution to water scarcity and electricity shortage. Here, we design a thermoelectricity–freshwater cogenerator based on a thermoelectric generator (TEG) and a starch–polyacrylamide (S-PAM) hydrogel to make the maximum use of solar energy and scavenging energy. A commercial $TiNO_x$ blue membrane with high absorptance and low emissivity covers the hot side of the TEG, which is used as the solar absorber for the main energy input. The S-PAM hydrogel underneath the cold side of TEG uses waste heat for evaporation, constituting the multistage utilization of solar energy. The temperature of the evaporation surface drops below the environmental temperature by the optimization of heat transfer channels at the cold side, resulting in a net energy gain from the environment. Simultaneously, the S-PAM hydrogel possessing a hydrophilic and porous 3D network can accommodate much water to absorb heat at the cold side of TEG during the evaporation of water, which creates a large temperature difference between the two sides of TEG and thus in turn, elevates the thermoelectricity performance. The conductive heat loss from the purifier to bulk water is fully eliminated by spraying water and the rapid heat exchange occurs at the cold side of the TEG, which results in further electricity enhancement. Due to the utilization of the scavenging energy, our hybrid cogenerator obtains an evaporation rate of $1.79 \text{ kg m}^{-2} \text{ h}^{-1}$ and a record maximum output power density of 11.39 W m^{-2} during water spraying for 2 minutes under one-sun illumination in reported cogeneration systems based on TEGs. Therefore, ours is a pioneering study on a highly efficient and sustainable way to harvest solar and scavenging energy.

1. Introduction

A booming global population and the rapid development of society has led to environmental pollution and the shortage of fossil fuels, which exert a tremendous load on drinking water

[a] *Guangxi Key Laboratory of Information Material, Engineering Research Center of Electronic Information Materials and Devices, Ministry of Education, School of Material Science and Engineering, School of Mechanical and Electrical Engineering, Guilin University of Electronic Technology, Guilin 541004, P. R. China. E-mail: miaolei@guet.edu.cn*

[b] *Department of Chemical Systems Engineering, Graduate School of Engineering, Nagoya University, Nagoya, 464-8603, Japan*

[c] *College of Arts and Science, University of Tokyo, Tokyo 1538902, Japan*

[d] *International Center for Materials Nanoarchitectonics (WPI-MANA), National Institute for Materials Science (NIMS), Namiki 1-1, Tsukuba 305-0044, Japan. E-mail: mori.takao@nims.go.jp*

[e] *Graduate School of Pure and Applied Sciences, University of Tsukuba, 1-1-1 Tennodai, Tsukuba, Ibaraki 305-8577, Japan*

† Electronic supplementary information (ESI) available. See DOI: https://doi.org/10.1039/d2ee01394k

and electricity supplies. The global challenge within the water–energy nexus is a key impediment to the sustainable development of human society in the 21st century.[1–3] It is estimated that by 2025, more than two-thirds of the world's population will face severe imbalances between water requirements and supplies, especially in Asia and Africa.[4] Following the sustainable development, various green energy sources have been researched to produce electricity (piezoelectricity,[5–7] wind power generation,[8] hydro power,[9] photovoltaics,[10–12] and thermoelectricity[13–16]) and freshwater (reverse osmosis,[17] ion exchange,[18] catalytic oxidation,[19–21] and solar evaporation[22–26]). However, separate development inevitably causes high costs, low energy utilization efficiency and a large footprint to achieve both goals. Notably, the free and inexhaustible solar energy as intersectional energy for both is promising to solve the intertwined challenge posed by water and power.

In the reported studies of simultaneous freshwater and electricity generators (SFEGs), many defects, such as salt plugging, low output power and fragile climate adaptation hinder their synergistic applications.[27–34] Besides, the conductive heat

3388 | *Energy Environ. Sci.,* 2022, **15**, 3388–3399

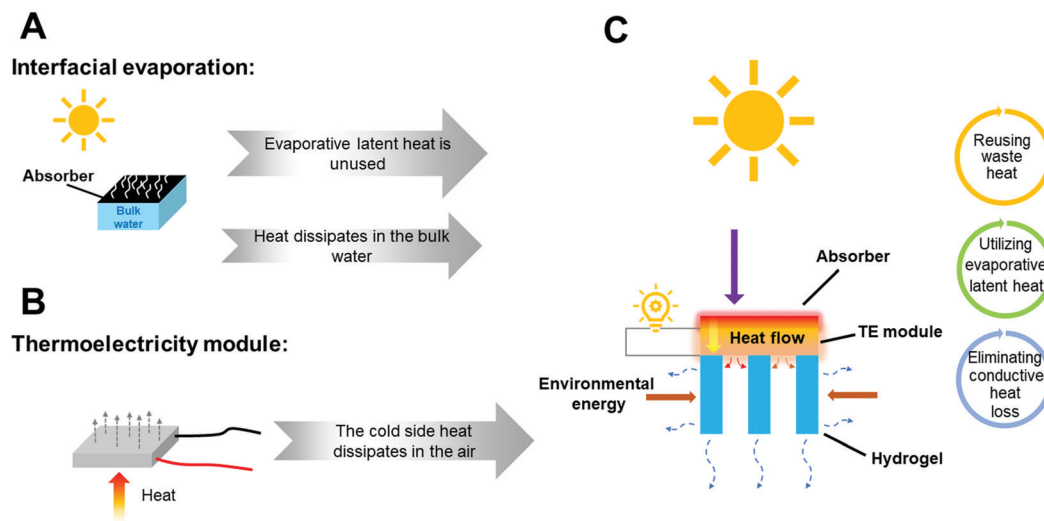This journal is © The Royal Society of Chemistry 2022

Fig. 1 The diagram of the TEG, interfacial evaporation and proposed hybrid cogenerator for electricity and water. (A) The diagram of interfacial evaporation. (B) The diagram of the TEG. (C) The diagram of the proposed hybrid cogenerator for electricity and water.

loss from the purifier to the bulk water severely decreases energy utilization efficiency, and the evaporative latent heat aspect is unexploited (Fig. 1A). Therefore, designing a cogeneration system possessing the potential of continuity and wide climate adaptability remains a challenge.

Thermoelectric generators (TEGs) generating power *via* Seebeck are conventionally embraced as the most suitable devices for waste heat recovery.[35] TEGs can produce electricity anywhere where there is a temperature difference created between two sides. It is a promising candidate for the cogeneration system because of its excellent adaptability to various working conditions. But in reported research studies about TEGs,[36,37] in order to achieve a high output power, extra-accessories (*e.g.* heatsink and radiative cooler) are introduced to directly or indirectly dissipate the heat at the cold side (Fig. 1B), leading to energy waste. Therefore, it is highly desirable to utilize scavenging energy to improve the performance of SFEGs.

The passive heat management in the utilization of latent heat with phase change has been studied for long time. Phase change materials (PCMs) can absorb or release heat, known as latent heat, during the phase-change process. Some solid–liquid PCMs, such as paraffin waxes, salt hydrates, and fatty acids can absorb latent heat during melting, thus obtaining desired heat dissipation in some applications.[38] However, their comparatively low phase change enthalpies have limited their wide application. Hydrogel with a hydrophilic 3D matrix can accommodate lots of water to absorb heat during the liquid–vapor phase change of water. The high phase change enthalpy of water drives the hydrogel as a promising alternative to dissipate heat. However, since the total water content of the hydrogel is limited, fast water uptake and supply is very important to long-term heat dissipation.

Owing to non-toxicity, good biocompatibility, broad accommodation in a porous matrix, and satisfactory chemical stability, the polyacrylamide (PAM) hydrogel has been favored in many fields, such as tissue engineering, drug delivery, and soft machines.[39,40] Here, we present a novel thermoelectricity–water

cogenerator based on a TEG and starch–polyacrylamide (S-PAM) hydrogel by using solar energy and scavenging energy. The TEG is placed at the middle of the cogenerator to generate electricity (Fig. 1C). A $TiNO_x$ blue membrane (BM) at the top with high absorptance is used as the solar absorber for the main energy input. The S-PAM hydrogel is used as the purifier underneath the cold side of TEG to generate vapors *via* liquid–vapor phase change using waste heat. During evaporation, the latent heat with phase change is utilized to regulate the thermal behavior and the temperature at the cold side of TEG can be reduced, thus promoting thermoelectricity performance. An intermittent spray is adopted for fast water supply to ensure long-lasting effective freshwater generation and thermal regulation. It prevents the conduction heat loss from the contact between the purifier and the bulk water, and provides a rapid heat exchange at the cold side to further enhance the output power. The heat transfer channel at the cold side of TEG is optimized to fully use waste heat and gain net energy from the environment by changing the shapes and geometries of the developed hydrogel. With the help of the scavenging energy including latent heat with phase change, net energy gain from the environment, waste heat at the cold side and eliminated conductive heat loss, our proposed hybrid cogenerator provides an evaporation rate of 1.79 kg m^{-2} h^{-1} and an amazing maximum output power density of 11.39 W m^{-2} during water spraying for 2 minutes under one-sun illumination. Besides, a maximum output voltage of 3.96 V and a water collection rate of 0.92 kg m^{-2} were obtained under natural sunlight in 8 hours. The strategy of such a scavenging energy scheme is expected to be widely adopted in simultaneous water and electricity generation in the future.

2. Results and discussion

2.1. Design principle and synthesis of the S-PAM hydrogel

To simultaneously realize efficient evaporation and electricity yield, the solar energy and the scavenging energy are focused on

This journal is © The Royal Society of Chemistry 2022

Energy Environ. Sci., 2022, **15**, 3388–3399 | **3389**

the development of the hybrid cogenerator. Passive thermal management using latent heat with phase change of water in the hydrogel is highly efficient because of its high phase change enthalpy. However, as the phase change persists, the freshwater generation and passive cooling effect decrease due to the lack of liquid water, leading to blocked sewage treatment and invalid heat management until the next reload. The spray that is utilized can not only supply enough water for hydrogel in time but also promote electrical performance by providing rapid heat exchange at the cold side of TEG. More strikingly, from the perspective of energy utilization, conductive heat loss from the purifier to bulk water could be fully eliminated using spray by avoiding the contact of both. In order to have better synergy with spraying, some characteristics such as strong robustness and fast water uptake capacity are necessary for the purifier and passive thermal regulator that we developed.

Benefitting from the broad accommodation in porous matrix and excellent hydrophilicity, the PAM is selected as the skeleton of the purifier in this paper. However, the pure PAM hydrogel is too brittle to be used as a purifier in harsh work environments that undergo an external force like spraying. Therefore, organic macromolecular material soluble starch which possesses many hydroxyl groups was introduced to strengthen the skeleton of the PAM hydrogel and the hydrophilicity. The S-PAM hydrogel was synthesized using a free radical polymerization method depicted in Fig. 2A. The S-PAM hydrogel with a tailorable and flexible performance is used in our strategy as a scavenger for purification and cooling.

As shown in SEM image of Fig. 2B, the internal skeleton of pure PAM hydrogel is thin and weak. After the introduction of starch, the morphology of S-PAM hydrogel changes to become thick and strong (Fig. 2C), which can provide protection against external forces. The relatively perturbation-resistant performance of the S-PAM hydrogel is shown in Video S1 (ESI†). The S-PAM hydrogel could withstand continuous perturbations under 500 g weight. Besides, the S-PAM hydrogel possesses excellent resilience after an approximately 120° folding (as shown in Video S2, ESI†). These excellent mechanical properties
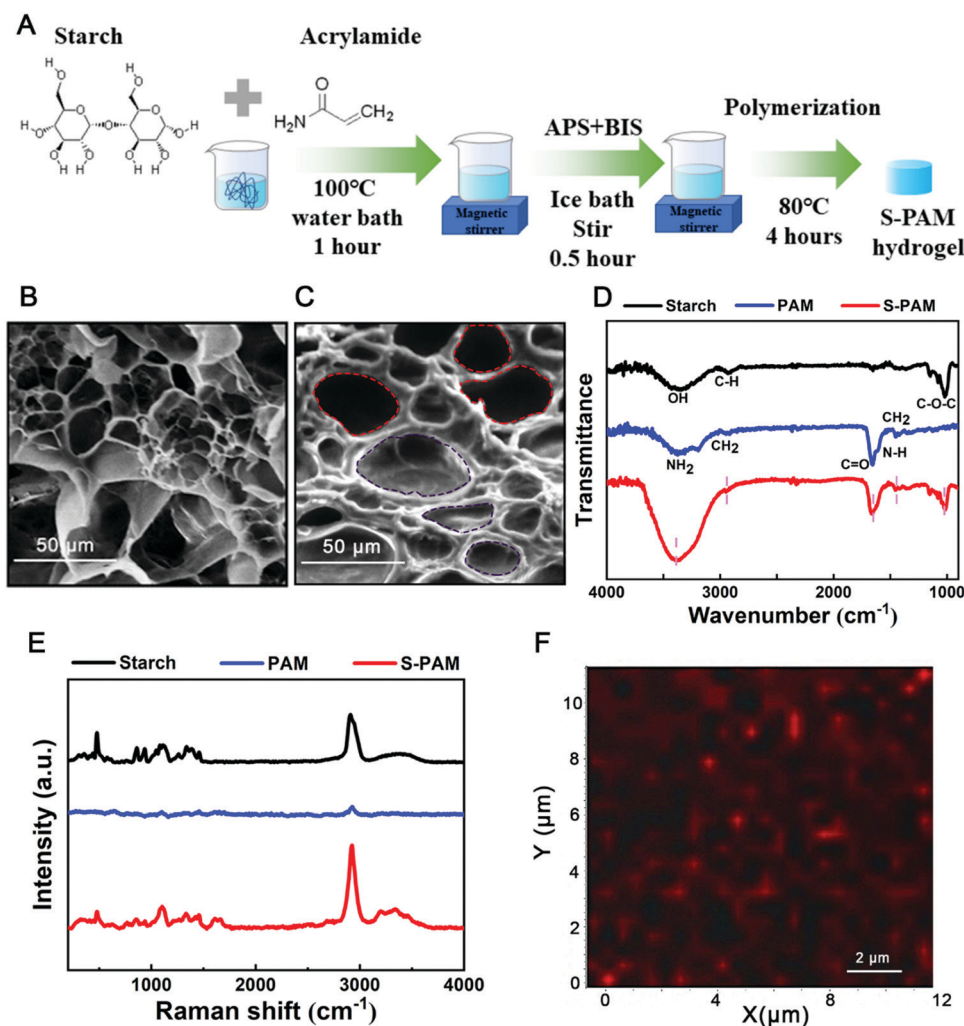

Fig. 2 Characterizations of S-PAM hydrogel. (A) The schematic diagram of S-PAM hydrogel synthesis. (B) The scanning electron microscope (SEM) image of the PAM hydrogel. (C) SEM image of S-PAM hydrogel. (D) The FTIR spectra of starch, PAM, and S-PAM hydrogels. (E) The Raman spectra of starch, PAM, and S-PAM hydrogels by point scanning. (F) The Raman spectra of the S-PAM hydrogel by mapping scanning.

can ensure the desired compatibility between the S-PAM hydrogel and spray.

As shown in Fig. 2D, Fourier transform infrared (FTIR) spectra distinctly display the types and origins of functional groups. The S-PAM has a broad peak from 3027 cm^{-1} to 3688 cm^{-1} originating from the hydroxyl groups of starch ($\sim$3392 cm^{-1}) and amidogen groups of PAM ($\sim$3193.68 cm^{-1} and 3377.37 cm^{-1}). The characteristic peaks of 1444.97 cm^{-1} and 2944.89 cm^{-1} are caused by the stretching vibrations of hydrocarbons. The peaks of 1653.24 cm^{-1} and 1607.45 cm^{-1} correspond to C$=$O and N–H of PAM, respectively. The S-PAM has C–O–C stretching vibration absorption peak (triplet: 1153.27 cm^{-1}, 1083.36 cm^{-1}, 1021.17 cm^{-1}). The introduction of hydrophilic groups –OH in the pure PAM hydrogel is expected to enhance the wetting properties for fast water uptake during spraying. The Raman spectra of starch, PAM, and S-PAM are also characterized. As shown in Fig. 2E, the characteristic peaks of the composite S-PAM hydrogel are coincident with those of starch and PAM. Besides, during the spraying process, water is uniformly supplied by a sprinkler, and thus the hydroxyl groups from starch will directly influence the water distribution. Local water accumulation caused by gathering of hydroxyl groups will lead to abnormal heat transfer and evaporation behavior. To evaluate the uniformity of hydroxyl groups in the composite, the peak of starch (478.51 cm^{-1}) is chosen as the characteristic peak for Raman mapping. As shown in Fig. 2F, the red regions are homogeneously dispersed on the surface of the S-PAM hydrogel indicating that the distribution of hydroxyl groups in S-PAM is well-proportioned.

The water contact angles (WCAs) of different evaporation surfaces which represent water uptake speed and reflect the bonding force of water are tested and recorded. The TEGs are packaged in alumina ceramics (WCA of $\sim$93.28° after 10 s, Fig. S1A, ESI†) which protect the TEG from water vapor corrosion generated by the bottom purifier. The WCA of air-laid paper is 0° after 1.25 s (Fig. S1B, ESI†), indicating that it can provide more water to be evaporated than that of pristine TEG. The –OH and –NH$_2$ in starch and acrylamide make the S-PAM hydrogel hydrophilic. As shown in Fig. S1C (ESI†), the S-PAM (WCA of 0° after 0.8 s) presents stronger wetting property, enabling the water to be continuously evaporated for the cogenerator. Fig. S2 (ESI†) shows the WCAs of different hydrogels, revealing that the S-PAM hydrogel possesses a faster water uptake speed than those of other hydrogels. The excellent water uptake capacity leads to more water in hydrogels under identical water supply, thus producing a more prominent cooling effect than those of other hydrogels (Fig. S3, ESI†). Therefore, the S-PAM hydrogel can ensure the continuous evaporation of water even without any assistance of water transportation path (e.g. air-laid paper and sponge) and fast water uptake during spray. The appropriate wetting properties further improve compatibility between the S-PAM hydrogel and the spray. This strategy and mechanisms of the S-PAM hydrogel and the spray can be useful for other applications as well.

2.2. Utilizing the waste heat at the cold side of the TEG and environmental energy for evaporation

It is essential to make the main energy input covering the absorber of TEG hot side. TiNO$_x$ BM possesses not only high absorptance (Fig. S4, ESI†, $\sim$93.55%) from 250 to 2500 nm and thermal conductivity but also low emissivity, thus being able to
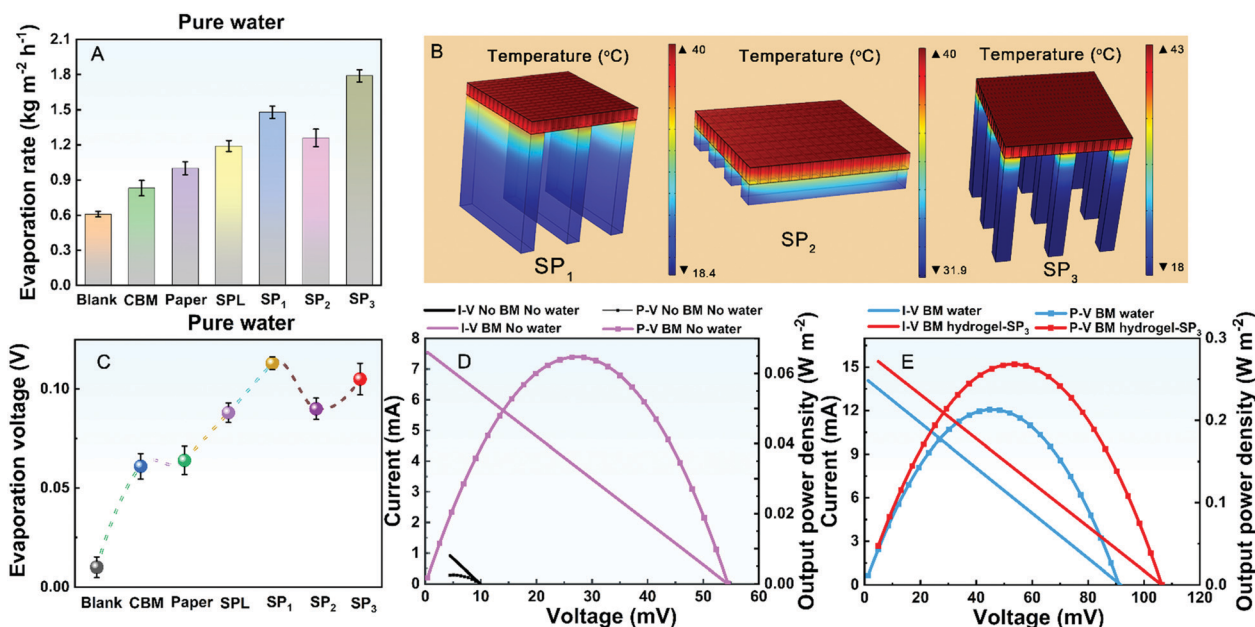

Fig. 3 The evaporation, temperature simulation, and electricity performances of the hybrid cogenerators. (A) The evaporation performances of cogenerators for DI water under 1 kW m^{-2} illumination. (B) The temperature simulations of SP$_1$-type, SP$_2$-type and SP$_3$-type cogenerators. (C) The evaporation voltages of different hybrid cogenerators for DI water under 1 kW m^{-2} illumination. (D) The curves of current–voltage (I–V) and output power density–voltage (P–V) of with and without BM under 1 kW m^{-2} illumination. (E) The curves of current–voltage (I–V) and output power density–voltage (P–V) of different hybrid cogenerators under 1 kW m^{-2} illumination.

This journal is © The Royal Society of Chemistry 2022

Energy Environ. Sci., 2022, **15**, 3388–3399 | **3391**

retain solar energy. As shown in Fig. 3A, the evaporation rate of a pristine TEG (Blank) is only 0.61 kg m^{-2} h^{-1} under 1 kW m^{-2} illumination. After covering the BM (denoted as the CBM hybrid model) at the hot side of TEG, the evaporation rate rises up to 0.83 kg m^{-2} h^{-1} due to the increased energy input. However, owing to thermal diffusion, there is much waste heat dissipating from the blank cold side to the air. To improve the utilization efficiency of waste heat, purifiers with water storage capacity are introduced at the cold side of the TEG (namely, air-laid paper and S-PAM hydrogel). As more waste heat is used, the experimental evaporation rates of TEG with air-laid paper (denoted as the Paper hybrid model) and S-PAM hydrogel layer (denoted as SPL hybrid model, with the thickness of ∼1 mm) are increased to 1 kg m^{-2} h^{-1} and 1.19 kg m^{-2} h^{-1}, respectively. As mentioned above, the waste heat at the cold side can be further exploited. Therefore, the heat transfer channels based on hydrogels with different geometries at the cold side of TEG are optimized, noted as SP$_1$, SP$_2$, and SP$_3$ hybrid models (as shown in Fig. S5, ESI†). Three different hybrid models based on various heat transfer channels are built using the COMSOL Multiphysics software to simulate the heat transfer process. The simulated temperature distributions of different hybrid models are shown in Fig. 3B. The optimization of heat transfer channels induces temperature dual-zones (taking the ambient temperature as the standard) represented in SP$_1$ and SP$_3$ hybrid models, demonstrating that the waste heat at the cold side has been fully used. Moreover, the blue zone in SP$_1$ and SP$_3$ where the temperature is lower than that of ambient temperature can further absorb environmental energy for evaporation. However, the phenomenon without a low temperature zone is shown in the simulated results of SP$_2$.

To verify the results of the waste heat utilization, the real hybrid cogenerators were established and their evaporation performances were tested. As shown in Fig. 3A, their evaporation rates of SP$_1$ (1.48 kg m^{-2} h^{-1}) and SP$_3$ (1.79 kg m^{-2} h^{-1}) are higher than that of SP$_2$ (1.26 kg m^{-2} h^{-1}) under 1 kW m^{-2} illumination owing to the different degrees of waste heat utilization at the cold side, consistent with the simulated results of heat transfer. It is noted that the evaporation rate of SP$_3$-type cogenerator reaches up to 1.79 kg m^{-2} h^{-1}, which is about three times that of the pristine TEG, suggesting the importance of scavenging energy.

2.3. Utilizing the latent heat with phase change of the S-PAM hydrogel for thermoelectric performance enhancement

Utilizing the latent heat with phase change of PCMs is a promising method for heat management of electronics. The PCMs can release or absorb thermal energy by changing their phases. The phase change of water is a highly effective strategy to boost the energy efficiency of semiconductor devices because of its high phase change enthalpy.[41] Therefore, appropriate coupling of S-PAM hydrogel and TEG can lead to mutual promotion. In our hybrid cogenerator, water in the S-PAM hydrogel can quickly evaporate using waste heat at the cold side of TEG and the evaporative latent heat can be utilized to decrease the temperature of the cold side, thus resulting in the enhancement of electricity in turn. The output voltages of SP$_1$,

SP$_2$, and SP$_3$ hybrid models have been simulated by the COMSOL Multiphysics software (Fig. S6, ESI†).

The output voltage of the hybrid cogenerator shows two different enhancement states when the spray turns on and off. To comprehensively evaluate the electrical performance, two parameters, evaporation voltage (spray off) and spraying voltage (spray on), were tested and analyzed (see more test details in the ESI†) in the practical experiment. As shown in Fig. 3C, the evaporation voltage of the pristine TEG is only 0.01 V under 1 kW m^{-2} illumination. The evaporation voltage of the CBM hybrid model increases to ∼0.06 V due to increased energy input. When adding the dry air-laid paper at the cold side of TE generator, the evaporation voltage is almost unchanged because there is no extra energy input. When the cold side of the TEG is decorated by the S-PAM layer, the evaporation voltage increases to ∼0.09 V because of the evaporative cooling effect caused by water in hydrogel itself. With the change of the heat transfer channel, the evaporation voltage is further improved. The evaporation voltages of SP$_1$, SP$_2$, and SP$_3$ are 0.113 V, 0.09 V, and 0.105 V, respectively, which are similar to the simulated values. The evaporation voltages of SP$_1$, SP$_2$, and SP$_3$ produce about 1030%, 800%, and 950% enhancements compared with that of pristine TEG, benefitting from the return effect of water evaporation.

To further reveal the importance of latent heat with the phase change of the S-PAM hydrogel for output power, the current–voltage (I–V) characteristics and output power density–voltage (P–V) curves of different hybrid cogenerators under steady conditions are plotted. As shown in Fig. 3D, the open-circuit voltage of the pristine TEG (no BM, no water supply) is ∼10 mV and the short-circuit current is ∼1.5 mA under 1 kW m^{-2} illumination, resulting in a maximum output power density of 0.0025 W m^{-2}. After being covered by BM (BM without water), the maximum output power density has been significantly improved to 0.0647 W m^{-2} (∼26 times that of the pristine TEG), resulting from the effect of BM on the solar energy harvesting. After introduction of evaporation at the cold side (BM with water), as shown in Fig. 3E, the maximum output power density has been further improved to ∼0.2129 W m^{-2} (∼85 times that of the pristine TEG). This is because the latent heat with phase change of water has been utilized at the cold side of TEG. When using the SP$_3$ hybrid model with optimized heat transfer channel, the maximum output power density of ∼0.2682 W m^{-2} has been obtained (∼107 times that of the pristine TEG). All of these phenomena show the return enhancement on electricity generation by utilizing latent heat of water evaporation in the S-PAM hydrogel.

The spray that is utilized can not only supply water for the purifier to ensure long-lasting effective thermal regulation but also provide a rapid heat exchange at the cold side of TEG. When water is sprayed to the cold side, a rapid heat exchange occurs there. The spraying voltages of different hybrid models during the rapid heat exchange process are recorded to comprehensively evaluate the electrical property. As shown in Fig. S7 (ESI†), in the case of spraying deionized (DI) water, the spraying voltage of the pristine TEG (without BM) is only

$\sim$0.04 V under 1 kW m^{-2} illumination because of low energy input. After the covering of BM and introduction of purifier, their spraying voltages have been promoted to $\sim$0.4 V and 0.28 V, respectively. The difference is caused by different exposed areas of the cold side. When water is sprayed to the cold side, it is easier and better to experience heat exchange between the bare cold side with sprayed water, causing a higher spraying voltage. Therefore, the relationships between spraying voltages and the exposed areas of the cold sides of SPL, SP$_1$, SP$_2$, and SP$_3$ were investigated and compared in Table S1 (ESI†).

Furthermore, the spraying rate could affect electrical performance. As shown in Fig. S8 (ESI†), the spraying voltages of the SP$_3$ hybrid model at different spraying rates have been measured and recorded. When the spraying rate is lowered, the spraying voltage is significantly decreased owing to reduction in the degree of heat exchange. However, according to energy matching in evaporation process,[22] too fast a spraying rate would suppress the evaporation, leading to reduction in freshwater production in our hybrid cogenerator. The water supplied by spray can directly cut off the contact between the purifier
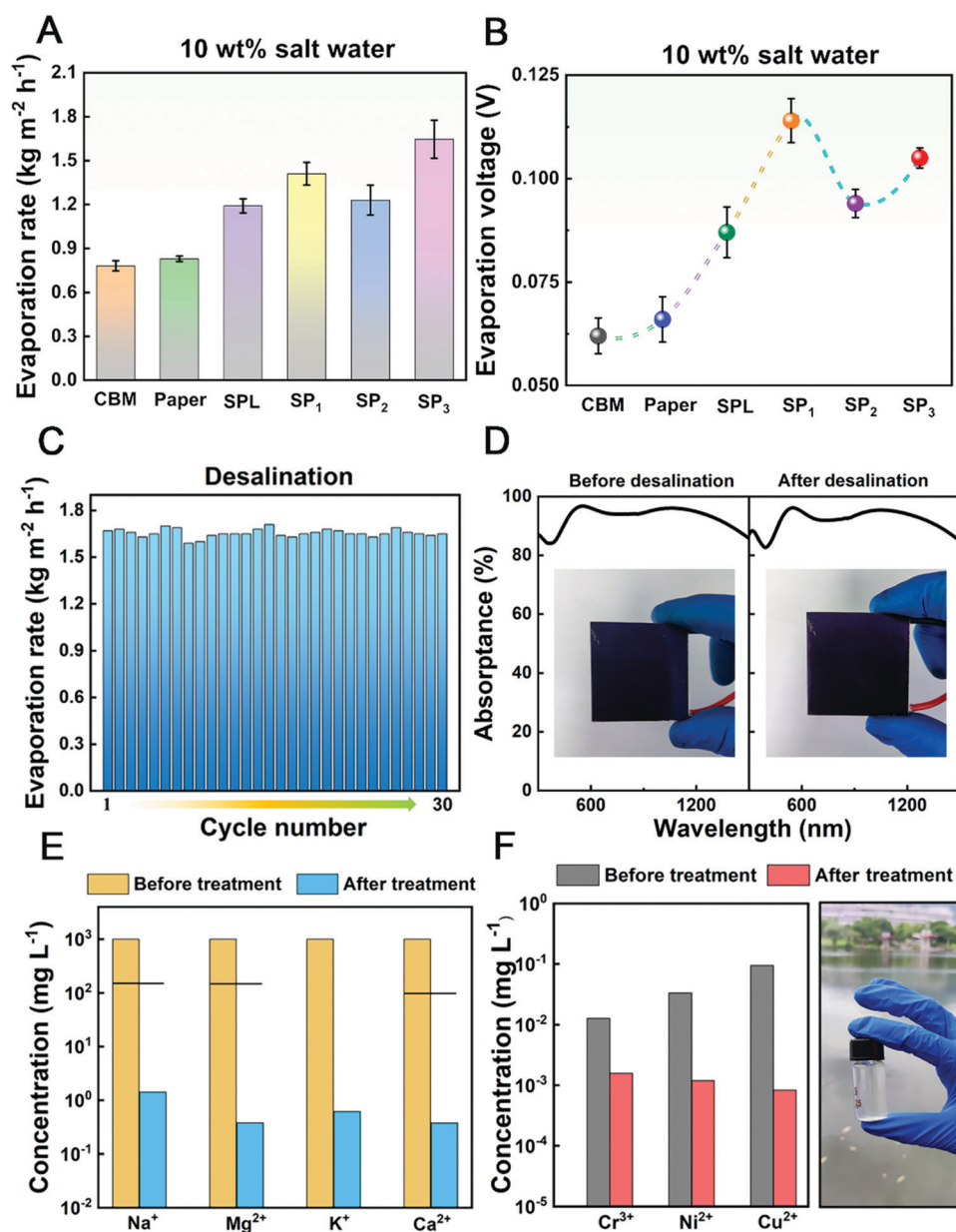

Fig. 4 The performances of desalination and treating other water sources. (A) The evaporation performances of cogenerators for 10 wt% salt water under 1 kW m^{-2} illumination. (B) The evaporation voltages of different hybrid cogenerators for 10 wt% brine under 1 kW m^{-2} illumination. (C) The circulation performance for 10 wt% brine of SP$_3$-type cogenerator under 1 kW m^{-2} illumination. (D) The absorptance and digital photos of BM before and after cyclic desalination. (E) Concentrations of four ions (Na$^+$, Mg^{2+}, K$^+$, Ca^{2+}) in self-configuration solution before and after treatment. The black line is the World Health Organization (WHO) standard of ion concentrations for drinking water. (F) Concentrations of three ions (Cr^{3+}, Ni^{2+}, Cu^{2+}) in Xiangsi Lake water before and after treatment.

This journal is © The Royal Society of Chemistry 2022

Energy Environ. Sci., 2022, **15**, 3388–3399 | **3393**

and the bulk water in space, resulting in the elimination of conductive heat loss.

Besides, a 100 Ω load is connected in series in the circuit to test the electrical performance. As shown in Fig. S9 (ESI†), the evaporation voltages and spraying voltages of CBM, Paper, and SP$_3$ are studied. The trends of evaporation voltage and the spraying voltage with 100 Ω (Fig. S9, ESI†) among CBM, Paper, and SP$_3$ are similar to those of no-load ones under 1 kW m^{-2} illumination (Fig. 3C and Fig. S7, ESI†). Note that the voltages with 100 Ω are slightly lower than those of no-load ones due to the partial voltage of internal resistance of the TEG.

2.4. Desalination and purification performance of the hybrid cogenerator

Desalination is essential for practical application of the hydrid cogenerator. So far, in most reported solar desalination devices, salt water is always transported to the surface of the photo-thermal material (PTM) owing to the integration of the purifier and the absorber.[42–44] Water evaporates from the upper surfaces of the PTM, but salt crystallizes and remains there. The accumulated salt severely affects the light absorption of PTM and hinders the escape of water vapor, thus reducing the efficiency of desalination. To solve this problem, we developed the hybrid cogenerator fully decoupling the absorber and the purifier. The BM as the solar absorber is kept at a distance (the height of pristine TEG) apart from the purifier, which protects the absorber from salt crystal precipitation. To evaluate desalination performance, 10 wt% NaCl solution is used for testing. As shown in Fig. 4A, the evaporation rates of CBM, paper, SPL, SP$_1$, SP$_2$, and SP$_3$ are 0.78, 0.83, 1.13, 1.41, 1.23, and 1.65 kg m^{-2} h^{-1}, respectively, under 1 kW m^{-2} illumination, which results from the varying utilization degrees of waste heat at the cold side caused by different heat transfer channels. Compared with DI water, the evaporation rates of 10 wt% salt water show slight decreases because of the difference in vapor pressure. The DI water has a higher vapor pressure than that of saline water, making it easier to evaporate from DI water.

The electrical property of the cogenerator for 10 wt% salt water has been tested. As shown in Fig. 4B, the evaporation voltages of CBM and paper hybrid models are similar (~ 0.06 V) due to the absence of evaporation cooling at the cold side of the cogenerator. After the introduction of the hydrogel purifier at the cold side, the evaporation voltages have increased (0.085 V for SPL, 0.110 V for SP$_1$, 0.089 for SP$_2$, and 0.103 V for SP$_3$), resulting from the utilization of latent heat with the phase change of water in the hydrogel. Besides, the voltages are nearly the same as those with hydrogel rich in DI water, indicating that salt water doesn't influence the electricity yield. As shown in Fig. S10 (ESI†), the curves of spraying voltages for 10 wt% salt water further validate the effect of exposed cold side area on the electrical performance.

Benefitting from the spray, the salt on the surface of the purifier can be washed off in time to solve the salt plugging problem while supplying water. To evaluate the long-term desalination performance of the hybrid cogenerator, 30 cycles and continuous desalination for 13 hours are carried out.

As shown in Fig. 4C, the evaporation rates for 30 cycles are stable and fluctuate around ~ 1.65 kg m^{-2} h^{-1}, exhibiting excellent cycling stability. The absorptances of BM before and after continuous desalination for 13 hours are nearly unchanged and remain at $\sim 93.55\%$ (as shown in Fig. 4D). Moreover, due to the separation between absorber and purifier, no salt crystals precipitate on the surface of BM after 13 hours of continuous desalination, indicating excellent stability to work for long periods nonstop.

In addition to 10 wt% salt water, two different water sources (self-configuring solution and Xiangsi Lake water) were investigated as sewage. After treatment, the concentrations of four primary ions (Na$^+$, Mg^{2+}, K$^+$, and Ca^{2+}) in the self-configuration solution decreased by three orders of magnitude, which could reach the World Health Organization (WHO) standards for drinking water (Fig. 4E). As for Xiangsi Lake water, three heavy metal ions (Cr^{3+}, Ni^{2+}, and Cu^{2+}) were detected. As shown in Fig. 4F, after treatment, heavy metal ions are also noticeably reduced.

2.5. Calculation of energy exchange in thermoelectricity–freshwater cogenerator

The degree of energy utilization in the hybrid cogenerator affects the performance of evaporation and electricity yield. To accurately characterize and calculate energy exchange of different hybrid models based on various heat transfer channels, the temperatures of hydrogels of three hybrid models (SP$_1$, SP$_2$, and SP$_3$) were recorded. The bottom temperature of SP$_1$, SP$_2$ and SP$_3$ type cogenerators under 1 kW m^{-2} illumination are shown in Fig. 5A and Fig. S11A (ESI†). As for the side temperature, similar to the simulated temperature distributions, the SP$_1$ (Fig. S11B, ESI†) and SP$_3$ (Fig. 5B) type cogenerators show temperature dual-zones taking ambient temperature as the standard. The present low temperature zone (below ambient temperature) could not only ensure maximum exploitation of waste heat at the cold side and gain extra energy from the environment for evaporation but also continuously cool the cold side for thermoelectric enhancement. The detailed energy exchanges of different cogenerators are calculated and shown in Table 1. The net energy exchange result of SP$_2$ is negative, indicating an inadequate utilization of energy in the SP$_2$ hybrid model. Not surprisingly, a positive energy gain happens in SP$_1$ and SP$_3$ hybrid models, leading to excellent electricity yield and evaporation performances.

2.5.1. The input solar power for the whole system. The input solar power (P_{input}) could be calculated by the eqn (1):[45]

$$P_{input} = C_{opt} \times I \times A_{abs} \tag{1}$$

where C_{opt} is the optical concentration, I is intensity of direct insolation on the horizontally cross-sectional plane of the absorber (1 kW m^{-2}), and A_{abs} is the area of the absorber (projected area: 4×4 cm^2). Under 1 kW m^{-2} illumination, the input solar power of the water–electricity generator is 1.6 W.

2.5.2. Reflection loss on the surface of absorber. The reflection loss over the whole solar spectrum is calculated to be 0.1032 W.
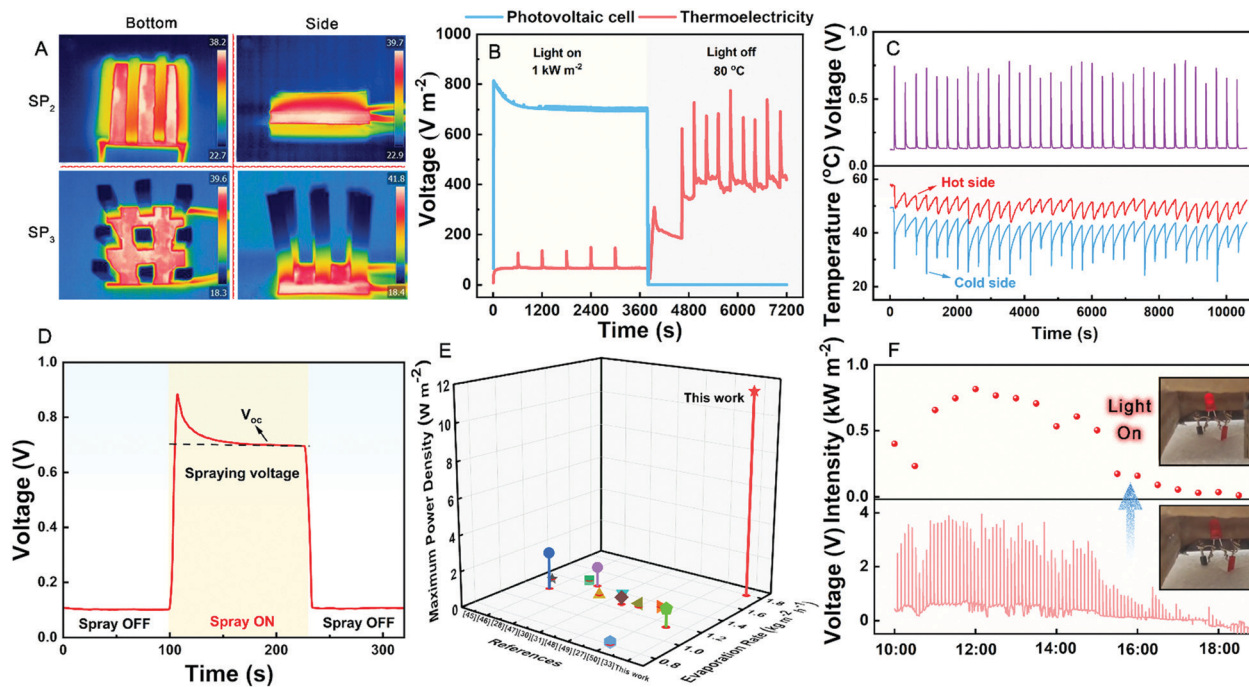
Fig. 5 The performance comparison and realistic home-made outdoor device. (A) The bottom and side temperatures of the SP$_2$-type and SP$_3$-type cogenerators under 1 kW m^{-2} illumination. (B) The electricity performance comparison of photovoltaic cells and thermoelectricity when light is on and off. (C) The synchronous curves of the output voltage and two side temperatures of TEG spraying 10 °C water under 1 kW m^{-2} illumination. (D) The output voltages of the hybrid cogenerator spraying 10 °C water for 2 min under 1 kW m^{-2} illumination. (E) The comparison of evaporation rate and maximum power density with reported works. (F) The outdoor solar light intensity and output voltage of the home-made device.

Table 1 The detailed heat flux of different hybrid cogenerators

Different hybrid cogenerators	BM (W)		Hydrogel bottom (W)		TE bottom (W)		Hydrogel side (W)			Total (W)
	Convection	Radiation	Convection	Radiation	Convection	Radiation		Convection	Radiation	
SP$_1$	−0.096	−0.0076	+0.017	+0.019	−0.021	−0.0085	Hot	−0.03	−0.035	
							Cold	+0.083	+0.094	+0.0149
SP$_2$	−0.096	−0.0076	−0.0085	−0.0099	−0.015	−0.0061		−0.041	−0.049	−0.2331
SP$_3$	−0.12	−0.0096	+0.01	+0.011	−0.025	−0.01	Hot	−0.024	−0.028	+0.2844
							Cold	+0.23	+0.25	

2.5.3. Radiation loss and convection loss of top BM. The radiation loss of top BM can be calculated using the Stefan–Boltzmann law:

$$P_{rad,BM} = A_{abs}\varepsilon_1\sigma(T_1^4 - T_2^4) \qquad (2)$$

where $P_{rad,BM}$ is the radiation loss of top BM, ε_1 is the emissivity of BM, σ is the Stefan–Boltzmann constant, T_1 is the environment temperature (28 °C) in evaporation experiment, and T_2 is the temperature of the BM.

The convection loss of top BM can be calculated by Newton's law of cooling:

$$P_{Con,BM} = A_{abs}\, h(T_1 - T_2) \qquad (3)$$

where $P_{Con,BM}$ is the convection loss of top BM, h is the convective heat transfer coefficient. To avoid the error caused by the temperature test, the average temperature was used for calculation.

2.5.4. Radiation loss and convection loss of the S-PAM hydrogel bottom (HB)

$$P_{rad,HB} = A_{HB}\, \varepsilon_2\, \sigma(T_1^4 - T_3^4) \qquad (4)$$

where $P_{rad,HB}$ is the radiation loss of the S-PAM hydrogel bottom, A_{HB} is the area of the S-PAM hydrogel bottom, ε_2 is the emissivity of the hydrogel, and T_3 is the bottom temperature of the S-PAM hydrogel.

$$P_{Con,HB} = A_{HB}h(T_1 - T_3) \qquad (5)$$

where $P_{Con,HB}$ is the convection loss of the S-PAM hydrogel bottom.

The bottom temperatures of the S-PAM hydrogels of SP$_1$-type, SP$_2$-type, and SP$_3$-type are 22.23 °C, 30.13 °C, and 18.8 °C, respectively. The bottom area of the S-PAM hydrogel for SP$_1$-type, SP$_2$-type, and SP$_3$-type are 6 cm^2 (4 × 0.5 × 3), 8 cm^2 (4 × 0.5 × 4), and 2.25 cm^2 (0.5 × 0.5 × 9), respectively.

This journal is © The Royal Society of Chemistry 2022

Energy Environ. Sci., 2022, **15**, 3388–3399 | **3395**

2.5.5. Radiation loss and convection loss of TE bottom (TB)

$$P_{\text{rad,TB}} = A_{\text{TB}}\varepsilon_3\sigma(T_4{}^4 - T_5{}^4) \tag{6}$$

where $P_{\text{rad,TB}}$ is the radiation loss of the TE bottom, A_{TB} is the area of the TE bottom, ε_3 is the emissivity of the TE surface, T_4 is the vapor temperature and T_5 is the temperature of the TE bottom.

$$P_{\text{Con,TB}} = A_{\text{TB}}h(T_4 - T_5) \tag{7}$$

where $P_{\text{Con,TB}}$ is the convection loss of the TE bottom.

The bottom temperatures of the TE of SP$_1$-type, SP$_2$-type, and SP$_3$-type are 38.4 °C, 37.53 °C, and 38.43 °C, respectively. The bottom area of the S-PAM hydrogel for SP$_1$-type, SP$_2$-type, and SP$_3$-type are 10 cm^2 ($4 \times 4 - 4 \times 0.5 \times 3$), 8 cm^2 ($4 \times 4 - 4 \times 0.5 \times 4$), and 13.75 cm^2 ($4 \times 4 - 0.5 \times 0.5 \times 9$), respectively.

2.5.6. Radiation loss and convection loss of the side S-PAM hydrogel.

The side temperature of the S-PAM hydrogel for SP$_2$-type is 32.6 °C. Its side area is 18 cm^2 (($4 \times 0.5 + 0.5 \times 0.5) \times 2 \times 4$). To accurately calculate the radiation loss and convection loss of the side S-PAM hydrogel, the side temperature of the S-PAM hydrogel for SP$_1$-type and SP$_3$-type are divided into two parts by the isotherm of 28 °C. The side temperature in high temperature zone (higher than 28 °C, SHH) of the S-PAM hydrogel for SP$_1$-type and SP$_3$-type are 31.7 °C and 32.4 °C, respectively. The side area of high temperature zone of S-PAM hydrogel for SP$_1$-type and SP$_3$-type are 16.2 cm^2 (($4 \times 0.6 + 0.5 \times 0.6) \times 2 \times 3$) and 10.8 cm^2 ($0.5 \times 0.6 \times 4 \times 9$), respectively. The side temperature in the low temperature zone (lower than 28 °C, SHL) of the S-PAM hydrogel for SP$_1$-type and SP$_3$-type are 23.6 °C and 20.6 °C, respectively. The side area of low temperature zone of the S-PAM hydrogel for the SP$_1$-type and SP$_3$-type are 37.8 cm^2 (($4 \times 1.4 + 0.5 \times 1.4) \times 2 \times 3$) and 61.2 cm^2 ($0.5 \times 3.4 \times 4 \times 9$), respectively.

The radiation loss of the high temperature zone:

$$P_{\text{rad,SHH}} = A_{\text{SHH}}\varepsilon_2\sigma(T_1{}^4 - T_6{}^4) \tag{8}$$

where $P_{\text{rad,SHH}}$ is the side radiation loss of S-PAM hydrogel in high temperature zone, A_{SHH} is the area of the side high temperature zone of S-PAM hydrogel, T_6 is the side temperature of the S-PAM hydrogel in the high temperature zone.

The convection loss in the high temperature zone:

$$P_{\text{Con,SHH}} = A_{\text{SHH}}h(T_1 - T_6) \tag{9}$$

where $P_{\text{Con,SHH}}$ is the side convection loss of the S-PAM hydrogel in the high temperature zone.

The radiation loss of low temperature zone:

$$P_{\text{rad,SHL}} = A_{\text{SHL}}\varepsilon_2\sigma(T_1{}^4 - T_7{}^4) \tag{10}$$

where $P_{\text{rad,SHL}}$ is the side radiation loss of the S-PAM hydrogel in the low temperature zone, A_{SHL} is the area of the side low temperature zone of the S-PAM hydrogel, and T_7 is the side temperature of S-PAM hydrogel in low temperature zone.

The convection loss in the low temperature zone:

$$P_{\text{Con,SHL}} = A_{\text{SHL}}h(T_1 - T_7) \tag{11}$$

where $P_{\text{Con,SHL}}$ is the side convection loss of the S-PAM hydrogel in the low temperature zone.

2.6. The performance comparison and outdoor cogeneration performance

Photovoltaic cells possess excellent practical electrical performance due to their direct conversion process, contributing to advancements in the water–electricity cogeneration field.[3,46] Although the cogeneration systems based on photovoltaic cells have reached unrivalled electricity yield on a clear day, the intermittency caused by day–night alternation and weather change is still an insurmountable challenge so far. TEGs can generate power via Seebeck effect anywhere where there is a temperature difference between the two sides. Its wide adaptability to work environments and feasibility place it in the spotlight. To compare the application potential under special conditions, the electrical properties of our SP$_3$-type cogenerator and photovoltaic cells with SP$_3$-type hydrogels were compared when light was on and off (Fig. 5B). Under a 1 kW m^{-2} simulated sunlight illumination, the voltage density of the photovoltaic cells is higher than that of our SP$_3$-type cogenerator because of the direct energy conversion process. However, when the light is off and an 80 °C heat source which simulates waste heat at night (e.g. hot pipe and high power device) is used, the thermoelectric performance remains excellent. In contrast, the photovoltaic cells are nearly disabled (with ~0 V m^{-2}). The results show that the cogeneration system using thermoelectricity possesses more extensive and wider adaptability potential than that using photovoltaic cells. Therefore, it is significant to develop the hybrid cogenerator based on TEG to relieve the water and energy nexus.

To better utilize the rapid heat exchange from spray, the output voltage and the two sides temperatures of TEG were synchronously measured (using 10 °C water). As shown in Fig. 5C, the maximum temperature difference of TEGs can reach up to 20–25 °C. The voltage of our hybrid cogenerator was recorded during spraying with 10 °C water for 2 min under 1 kW m^{-2} illumination (Fig. 5D). The maximum power density has been calculated by the equation:

$$\text{Maximum power density} = V_{\text{oc}}{}^2/(4R_{\text{TEG}}A_{\text{TEG}}) \tag{12}$$

where V_{oc} is the open circuit voltage during spraying, R_{TEG} is the total electrical resistance of the TEG, and A_{TEG} is the projected area of the TEG.

Fig. 5E and Table 2 list the properties of our thermoelectricity–freshwater cogenerator and other reported research studies for SFEGs, revealing excellent performance in our hybrid cogenerator, in particular, obtaining an amazing maximum output power density. Based on the hybrid model focusing on scavenging energy, a practical outdoor setup with nine hybrid modules and a water collection part was designed and constructed (Fig. S12, ESI:† the real setup). The body of the setup was made of transparent acrylic board. Nine hybrid TEGs with SP$_3$ models were connected in series. An automatic spraying module controlled using a computer program was assembled to supply water. The water collection part consisted of a spiraling

3396 | Energy Environ. Sci., 2022, **15**, 3388–3399

This journal is © The Royal Society of Chemistry 2022

Table 2 The comparison with other studies on simultaneous generation water and electricity

Materials	Solar intensity (kW m^{-2})	Water supply	Evaporation rate (kg m^{-2} h^{-1})	Maximum power density (W m^{-2})	Ref.
PDMS/CuO/Cu	1	2D	1.33	1.6×10^{-3}	47
PVDF/graphene	1	Direct contact	1.2	2.11	48
Cu-BTC coated with PANI	1	Direct contact	1.442	1.534×10^{-2}	28
Integrating TGC and RED	1	Direct contact	1.4	1.11	49
Au nanoflower	1	Direct contact	1.3	8.9×10^{-4}	30
Self-contained monolithic carbon sponges	1	Storage water	1.39	2.4×10^{-4}	31
Graphite/Nonwoven	8	Direct contact	4.2	0.9	36
Food-derived carbonaceous material	1	Direct contact	1.26	0.4	50
Ni$_3$S$_2$/NF	1	1D	1.29	0.175	51
MWNTs on the fiber layer-coated cellulose	1	1D	1.364	1.76×10^{-4}	27
CC-BPHPLS	1	1D	0.804	0.115	52
Filter paper modified by CNT	1	1D	1.15	1	33
This work	1	Spray	1.79	11.39	

water pipe and a water collector. Related hardware, including STM32F103, relay, and solenoid valve, were used to manipulate the water tap. The purified water could be collected through a spiral descending pipe attached to the inner wall of the body. Besides, the angle demodulator, including 0°, 10°, and 30°, was designed in the device to adjust for different solar incident angles (Fig. S13, ESI†). After the device continuously works for about 8 hours (10:00–18:00), the freshwater collection rate of 0.92 kg m^{-2}, and a maximum output voltage of 3.96 V are obtained, while the output voltage varies with natural sunlight (Fig. 5F). The voltage enhancement could directly light up an LED without any additional equipment such as a charge amplifier (insets of Fig. 5F). The real time status of the LED is shown in Video S3 (ESI†).

3. Conclusions

A novel thermoelectricity–freshwater cogenerator based on a TEG and a S-PAM hydrogel focusing on scavenging energy is designed and developed. Owing to the utilization of the scavenging energy (latent heat with phase change, net energy gain from the environment, waste heat at the cold side and eliminated conductive heat loss), cogeneration performances have been mutually promoted. The salt crystal precipitation caused by long-term continuous desalination has been eradicated by decoupling the absorber and the purifier. The hybrid cogenerator obtains a record maximum output power density of 11.39 W m^{-2} during spraying under one-sun illumination in the reported cogeneration system based on TEGs. The practical performances with a water collection rate of 0.92 kg m^{-2} and a maximum output voltage of 3.96 V are obtained in an 8 hour outdoor home-made setup. The approach with scalable, robust hydrogel and extreme energy exploitation will provide an attractive avenue for long-lasting and highly efficient electricity–freshwater cogeneration.

4. Experimental section

Materials

Starch, acrylamide (99%), ammonium persulfate, and *N,N'*-methylenebisacrylamide (99%) were purchased from Innochem.

Fabrication of the starch–polyacrylamide (S-PAM) hydrogel

The 0.7 g starch and 1 g acrylamide were added into deionized water (10 mL) and vigorously stirred in 100 °C water bath for an hour. When the solution cooled to room temperature, it was stirred in an ice bath for 10 minutes. Then 0.01 g ammonium persulfate (APS) and 0.1 g *N,N'*-methylene bisacrylamide (BIS) were added into the solution and vigorously stirred further for 0.5 hour. The solution was then poured into a prepared mold and polymerized at 80 °C for 4 hours. Finally, the S-PAM hydrogel was obtained.

Characterization methods

The morphologies and structure of the hydrogel were characterized by scanning electron microscopy (SEM QUANTA-450 FEG, Thermo Fisher, America) at an acceleration voltage of 10 kV. The water contact angles of hydrogels were recorded using a contact angle analyzer (JC2000D1, Powereach Co, China). The absorption spectra of the absorber were measured from 250 to 2500 nm using a UV/vis/NIR spectrometer (Lambda 750S with integrating sphere, PerkinElmer, USA). Real-time mass change was recorded by an electronic balance (ATX224, Shimadzu, Japan). The functional groups and characteristic peaks of samples were measured by FTIR spectroscopy (NICOLET IS10, Thermo Fisher Scientific, America) and Raman spectroscopy (HORIBA Lab RAM HR Evolution, France), respectively. The voltages generated by the cogenerators were recorded on a nanovoltmeter (Keithley, model 2182A, America). The thermal conductivities of samples were measured by Thermal Constants Analyser (Kaits, TPS 2500 S, Sweden). The surface temperatures of cogenerators were measured by an IR camera (FLIR, FLIR-E64501, America). Vapor temperatures were measured using a thermocouple (Saiertong, BD-DR704, China).

Electricity generating device

The commercial TEG module based on bismuth telluride (length 4 cm, width 4 cm) possessing ZT value of ~1 was selected as the electricity generating device.

Author contributions

L. M., T. M., and X. M. designed research. X. M., H. C., and T. Y. performed research. X. M. programmed. X. M., P. W.,

and J. Z. analyzed data. L. M., T. M., X. M., and S. C. wrote the paper.

Conflicts of interest

There are no conflicts to declare.

Acknowledgements

References

1 X. Liao, L. Chai, Y. Jiang, J. Ji and X. Zhao, *J. Cleaner Prod.*, 2019, **229**, 350–357.

2 X. Zhao, X. Liao, C. Zhang, X. Zhang, G. Mao, S. Zhang and M. R. Tillotson, *J. Environ. Manage.*, 2021, **286**, 112259.

3 W. Wang, Y. Shi, C. Zhang, S. Hong, L. Shi, J. Chang, R. Li, Y. Jin, C. Ong, S. Zhuo and P. Wang, *Nat. Commun.*, 2019, **10**, 3012.

4 J. Fang, S. Wang, Y. Zhang and B. Chen, *Energy Procedia*, 2019, **158**, 3872–3877.

5 R. Wang, Y. Hu, D. Shen, J. Ma, J. Li and J. Wen, *IEEE Trans. Ind. Electron.*, 2021, **68**, 2015–2023.

6 S.-D. Guo, W.-Q. Mu and Y.-T. Zhu, *J. Phys. Chem. Solids*, 2021, **151**, 109896.

7 X. Yao, M. Jiang, W. Li, H. Lu, L. Li and G. Rao, *J. Mater. Sci.*, 2020, **31**, 21971–21980.

8 A. R. de Andrade, V. F. M. B. Melo, D. B. Lucena and R. Abrahão, *J. Braz. Soc. Mech. Sci. Eng.*, 2021, **43**, 182.

9 C. Condemi, D. Casillas-Pérez, L. Mastroeni, S. Jiménez-Fernández and S. Salcedo-Sanz, *Knowl.-Based Syst.*, 2021, **222**, 107012.

10 Y.-T. Huang, S. R. Kavanagh, D. O. Scanlon, A. Walsh and R. L. Z. Hoye, *Nanotechnology*, 2021, **32**, 132004.

11 J. J. Yoo, G. Seo, M. R. Chua, T. G. Park, Y. Lu, F. Rotermund, Y.-K. Kim, C. S. Moon, N. J. Jeon, J.-P. Correa-Baena, V. Bulović, S. S. Shin, M. G. Bawendi and J. Seo, *Nature*, 2021, **590**, 587–593.

12 Y. Li, L. Yu, L. Chen, C. Han, H. Jiang, Z. Liu, N. Zheng, J. Wang, M. Sun, R. Yang and X. Bao, *Innovation*, 2021, **2**, 100090.

13 Z. Liu, N. Sato, W. Gao, K. Yubuta, N. Kawamoto, M. Mitome, K. Kurashima, Y. Owada, K. Nagase, C.-H. Lee, J. Yi, K. Tsuchiya and T. Mori, *Joule*, 2021, **5**, 1196–1208.

14 M. Hong, W. Lyv, M. Li, S. Xu, Q. Sun, J. Zou and Z.-G. Chen, *Joule*, 2020, **4**, 2030–2043.

15 S. Perumal, M. Samanta, T. Ghosh, U. S. Shenoy, A. K. Bohra, S. Bhattacharya, A. Singh, U. V. Waghmare and K. Biswas, *Joule*, 2019, **3**, 2565–2580.

16 Y. Luo, S. Cai, S. Hao, F. Pielnhofer, I. Hadar, Z.-Z. Luo, J. Xu, C. Wolverton, V. P. Dravid, A. Pfitzner, Q. Yan and M. G. Kanatzidis, *Joule*, 2020, **4**, 159–175.

17 E. R. Cornelissen, D. J. H. Harmsen, B. Blankert, L. P. Wessels and W. G. J. van der Meer, *Desalination*, 2021, **509**, 115056.

18 M. A. C. K. Hansima, M. Makehelwala, K. B. S. N. Jinadasa, Y. Wei, K. G. N. Nanayakkara, A. C. Herath and R. Weerasooriya, *Chemosphere*, 2021, **263**, 127951.

19 H. Tan, P. Kong, R. Zhang, M. Gao, M. Liu, X. Gu, W. Liu and Z. Zheng, *Innovation*, 2021, **2**, 100089.

20 M. Pedrosa, J. L. Figueiredo and A. M. T. Silva, *J. Environ. Chem. Eng.*, 2021, **9**, 104930.

21 L. Zhang, Y. Zhang, J. Wei and W. Liu, *Chem. Eng. J.*, 2021, **403**, 126386.

22 X. Mu, Y. Gu, P. Wang, J. Shi, A. Wei, Y. Tian, J. Zhou, Y. Chen, J. Zhang, Z. Sun, J. Liu, B. Peng and L. Miao, *Sol. RRL*, 2020, **4**, 2000341.

23 J. Li, X. Wang, Z. Lin, N. Xu, X. Li, J. Liang, W. Zhao, R. Lin, B. Zhu, G. Liu, L. Zhou, S. Zhu and J. Zhu, *Joule*, 2020, **4**, 928–937.

24 P. Wang, X. Wang, S. Chen, J. Zhang, X. Mu, Y. Chen, Z. Sun, A. Wei, Y. Tian, J. Zhou, X. Liang, L. Miao and N. Saito, *ACS Appl. Mater. Interfaces*, 2021, **13**, 30556–30564.

25 Y. Gu, X. Mu, P. Wang, X. Wang, Y. Tian, A. Wei, J. Zhang, Y. Chen, Z. Sun, J. Zhou and L. Miao, *Global Challenges*, 2021, **5**, 2000063.

26 X. Mu, Y. Gu, P. Wang, A. Wei, Y. Tian, J. Zhou, Y. Chen, J. Zhang, Z. Sun, J. Liu, L. Sun, S. Tanemura and L. Miao, *Sol. Energy Mater. Sol. Cells*, 2021, **220**, 110842.

27 V.-D. Dao, *Sci. Total Environ.*, 2021, **759**, 143490.

28 Z. Li, X. Ma, D. Chen, X. Wan, X. Wang, Z. Fang and X. Peng, *Adv. Sci.*, 2021, **8**, 2004552.

29 S. Zhang, W. Chu, L. Li and W. Guo, *J. Phys. Chem. C*, 2021, **125**, 8959–8964.

30 M. Gao, C. K. Peh, H. T. Phan, L. Zhu and G. W. Ho, *Adv. Energy Mater.*, 2018, **8**, 1800711.

31 L. Zhu, M. Gao, C. K. N. Peh, X. Wang and G. W. Ho, *Adv. Energy Mater.*, 2018, **8**, 1702149.

32 Q. Shen, Z. Ning, B. Fu, S. Ma, Z. Wang, L. Shu, L. Zhang, X. Wang, J. Xu, P. Tao, C. Song, J. Wu, T. Deng and W. Shang, *J. Mater. Chem. A*, 2019, **7**, 6514–6521.

33 P. Yang, K. Liu, Q. Chen, J. Li, J. Duan, G. Xue, Z. Xu, W. Xie and J. Zhou, *Energy Environ. Sci.*, 2017, **10**, 1923–1927.

34 N. Xu, P. Zhu, Y. Sheng, L. Zhou, X. Li, H. Tan, S. Zhu and J. Zhu, *Joule*, 2020, **4**, 347–358.

35 G. Liu, T. Chen, J. Xu, G. Li and K. Wang, *J. Mater. Chem. A*, 2020, **8**, 513–531.

36 X. Li, X. Min, J. Li, N. Xu, P. Zhu, B. Zhu, S. Zhu and J. Zhu, *Joule*, 2018, **2**, 2477–2484.

37 A. P. Raman, W. Li and S. Fan, *Joule*, 2019, **3**, 2679–2686.

38 C. Wang, L. Hua, H. Yan, B. Li, Y. Tu and R. Wang, *Joule*, 2020, **4**, 435–447.

39 J. Zhou, Z. Sun, X. Mu, J. Zhang, P. Wang, Y. Chen, X. Wang, J. Gao, L. Miao and L. Sun, *Desalination*, 2022, **537**, 115872.

40 D. Zhao, M. Feng, L. Zhang, B. He, X. Chen and J. Sun, *Carbohydr. Polym.*, 2021, **256**, 117580.

3398 | *Energy Environ. Sci.*, 2022, **15**, 3388–3399

This journal is © The Royal Society of Chemistry 2022

41 S. Pu, J. Fu, Y. Liao, L. Ge, Y. Zhou, S. Zhang, S. Zhao, X. Liu, X. Hu, K. Liu and J. Chen, *Adv. Mater.*, 2020, **32**, 1907307.

42 S. Zhou, S. Huang, Y. Ming, Y. Long, H. Liang, S. Ruan, Y.-J. Zeng and H. Cui, *J. Mater. Chem. A*, 2021, **9**, 9909–9917.

43 Y. Sun, Z. Zhao, G. Zhao, L. Wang, D. Jia, Y. Yang, X. Liu, X. Wang and J. Qiu, *Carbon*, 2021, **179**, 337–347.

44 Y. Wang, X. Wu, T. Gao, Y. Lu, X. Yang, G. Y. Chen, G. Owens and H. Xu, *Nano Energy*, 2021, **79**, 105477.

45 J. Zhou, Y. Gu, P. Liu, P. Wang, L. Miao, J. Liu, A. Wei, X. Mu, J. Li and J. Zhu, *Adv. Funct. Mater.*, 2019, **29**, 1903255.

46 L. Yang, T. Sun, J. Tang, Y. Shao, N. Li, A. Shen, J. Chen, Y. Zhang, H. Liu and G. Xue, *Nano Energy*, 2021, **87**, 106163.

47 F. L. Meng, M. Gao, T. Ding, G. Yilmaz, W. L. Ong and G. W. Ho, *Adv. Funct. Mater.*, 2020, **30**, 2002867.

48 C. Huang, J. Huang, Y. Chiao, C. Chang, W. Hung, S. J. Lue, C. Wang, C. Hu, K. Lee, H. Pan and J. Lai, *Adv. Funct. Mater.*, 2021, **31**, 2010422.

49 H. Wang, W. Xie, B. Yu, B. Qi, R. Liu, X. Zhuang, S. Liu, P. Liu, J. Duan and J. Zhou, *Adv. Energy Mater.*, 2021, **11**, 2100481.

50 Y. Zhang, S. K. Ravi and S. C. Tan, *Nano Energy*, 2019, **65**, 104006.

51 H. Jiang, L. Ai, M. Chen and J. Jiang, *ACS Sustainable Chem. Eng.*, 2020, **8**, 10833–10841.

52 Y. Xu, Z. Guo, J. Wang, Z. Chen, J. Yin, Z. Zhang, J. Huang, J. Qian and X. Wang, *ACS Appl. Mater. Interfaces*, 2021, **13**, 27129–27139.

This journal is © The Royal Society of Chemistry 2022

Energy Environ. Sci., 2022, **15**, 3388–3399 | **3399**